



# Design and Testing of a Novel Piezoelectric-Driven Microvibration Hammerhead

Zhiyong Guo<sup>1</sup> · Zhemin Shen<sup>1</sup> · Weidong Liu<sup>1</sup> · Zhiqiang Zhang<sup>1</sup> · Lifeng Zhang<sup>1</sup> · Xuhao Wang<sup>1</sup>

Received: 2 December 2022 / Revised: 12 January 2023 / Accepted: 19 January 2023  
© The Author(s) 2023

## Abstract

A novel microvibration hammerhead consists of a piezoelectric actuator and a double cross-shape compliant mechanism (DCCM) is presented in this paper. The output force of the piezoelectric actuator can be detected in real time by an inside-installed pressure sensor. A theoretical model including the stiffness, first natural frequency, and stress of the DCCM and the displacement output of the piezoelectric actuator are established, and then they are further analyzed using the finite element analysis method. The effects of the beam thickness on the static and dynamic properties are deeply analyzed and compared. A prototype micro hammering system is constructed by integrating the microvibration hammerhead assembly and controlling system. Various experiments are also carried out to verify the basic performance of the micro hammering system.

## Highlights

1. A microvibration hammerhead including piezoelectric actuator, pressure sensor and DCCM was proposed.
2. The static and dynamic models of the DCCM were theoretically established, which was validated to be available in the analysis of the stiffness, stress and resonant frequency.
3. The relationships between the hammering force and initial contacting force, driving frequency and amplitudes were presented based on the experimental results.

**Keywords** Piezoelectric · Flexure hinge · Micro hammering

## 1 Introduction

High surface strength can help improve the abrasive resistance and fatigue properties of a component [1, 2]. The general surface-strengthening technique mainly includes deformation strengthening [3], cladding strengthening [4], and heat treatment [5]. Deformation strengthening applies mechanical force on a workpiece to produce microstructural change, refine grains, increase dislocation density, and further realize surface strengthening. The whole process is simpler and has a lower cost compared to other techniques. Based on the classical deformation strengthening technique,

vibration-assisted rolling has been proposed to further improve the strengthening effect, and many researchers have validated its efficiency [6, 7].

In the vibration-assisted rolling system, the microvibration system is the most important component, which is divided into resonant and non-resonant vibration systems. In the resonant vibration system, a transducer is generally selected to enlarge the vibration amplitude [8, 9]. However, the ultrasonic transmission is severely affected by the mechanical structure and clamping point, but the clamping point is not always calculated so accurately [10].

In the non-resonant vibration system, voice coil motors have the advantages of large stroke and high precision, and they have been utilized in vibration-assisted electrochemical machining [11]. However, a small output force is obviously not appropriate for the application of deformation strengthening. A piezoelectric ceramic displays high resolution, fast response, large stiffness, and output force, and it has been

✉ Zhiyong Guo  
zyguo@cauc.edu.cn

<sup>1</sup> College of Aeronautical Engineering, Civil Aviation University of China, Tianjin 300300, China

widely applied as an actuator in nanopositioning and vibration-assisted micro/nanomachining [12, 13]. Lu proposed a three-dimensional (3D) ultrasonic vibration platform with tunable characteristics, including vibration amplitude and frequency; the maximum amplitude and frequency reached approximately 50 nm and 20 kHz, respectively [14, 15]. Wang designed an ultrafast 2D nonresonant vibration cutting tool for machining microstructured surfaces, and the tool can operate at up to 6 kHz in a workspace of  $9.3 \times 16 \mu\text{m}$  [16]. Zhu developed a novel 2D vibration-assisted compliant cutting system with a parallel-kinematic configuration, which showed 494.4 and 697.5 Hz resonant frequencies in the  $X$ - and  $Y$ -directions, respectively [17]. All of these piezoelectric-driven and flexure hinge-supported vibration platforms were used to fabricate micro/nanostructures, but there have been no reports on the application of surface strengthening.

In this paper, a novel microvibration hammerhead is proposed, which mainly includes a piezoelectric actuator, the double cross-shape compliant mechanism (DCCM), and an inside-installed pressure sensor. The mechanical design of the microvibration hammerhead is first shown in Sect. 2. The theoretical stiffness, stress model of the DCCM, and displacement output model of the piezoelectric are established in Sect. 3. The finite element analysis (FEA) of the DCCM is implemented in Sect. 4. Lastly, a prototype micro hammering system is constructed and experimentally tested in Sect. 5.

## 2 Design of the Microvibration Hammerhead

As shown in Fig. 1, the microvibration hammerhead mainly includes a piezoelectric actuator, a pressure sensor, and the DCCM. A piezoelectric ceramic is employed to drive the

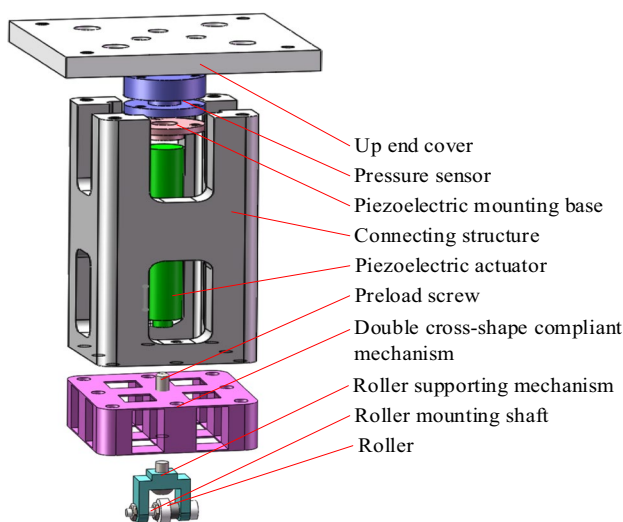


Fig. 1 Microvibration hammerhead

DCCM, and the output displacement of the piezoelectric is measured by a strain gauge mounted on the ceramic surface or an additional laser displacement sensor. The output force of the piezoelectric actuator is directly measured by the inside-installed pressure sensor. The preload screw and roller support mechanism are installed in the threaded center hole of the DCCM. The former is used to preload the piezoelectric actuator, whereas the latter is applied to support the roller. The roller is positioned by the right-hand round bush and further fixed by the left-hand nut in the mounting shaft. The connecting structure is used to connect these components together, and then the whole hammerhead is assembled on the base structure through the up-end cover.

During the micro hammering, the piezoelectric generates the vibration output and acts on the center rigid of the DCCM, and the DCCM pushes the roller rolling on the workpiece surface with a certain hammering force, which can be calculated in Eq. (1). The hammering force is mainly decided by the output displacement. A large stiffness of the pressure sensor is helpful in improving the hammering force.

$$F_{\text{ham}} = F_s - K_{\text{DCCM}}^{3,3} \left( s_0 - \frac{F_s}{K_s} \right), \quad (1)$$

where  $s_0$  is the output displacement of the piezoelectric actuator,  $F_s$  is the measured pressure,  $K_s$  is the stiffness of the

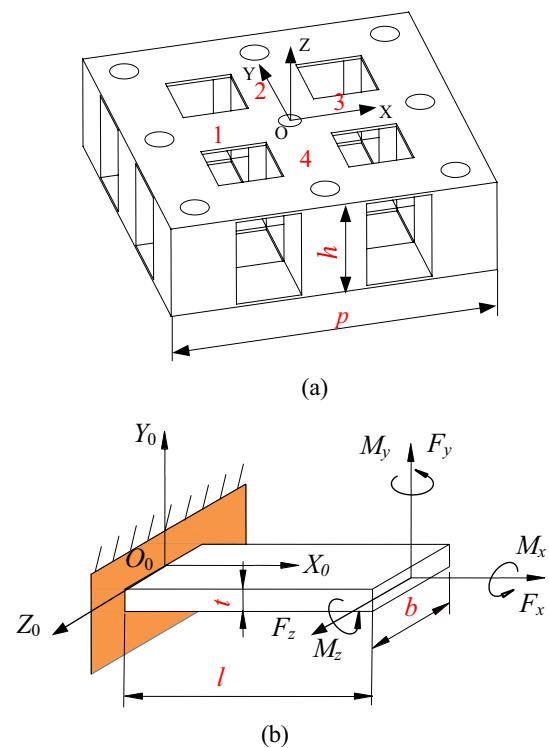


Fig. 2 Model of the probe suspension mechanism: **a** Cross-shape compliant mechanism; **b** Model of the leaf-spring flexure hinge

pressure sensor, and  $K_{DCCM}^{3,3}$  is the 3–3 element of the matrix  $K_{DCCM}$ ,  $K_{DCCM}$  is the stiffness of DCCM.

### 3 Theoretical Modeling

The DCCM plays an important role in the microvibration hammerhead, which suffers frequent deformations during hammering and supports the piezoelectric actuator and roller. Therefore, the theoretical analysis and FEA are implemented on it.

#### 3.1 Stiffness Modeling

As shown in Fig. 2a, the top and bottom compliant mechanisms of the DCCM are absolutely the same. For instance, the top layer includes 12 flexible beams, but only the central four beams generate deformation during the hammering because the surrounding rigid is fixed on the connecting structure; these four beams have been marked as 1–4 in Fig. 2a. Obviously, the four beams are overconstrained, but the movement along the Z-direction is free due to the flexibility of the beam in this direction. Simultaneously, the over-constraints in the other directions can help improve the dynamic property of the DCCM.

In the stiffness analysis of the DCCM, each flexible beam can be seen as a leaf-spring flexure hinge, which is modeled in Fig. 2b with the local coordinate  $O_0-X_0Y_0Z_0$ . According to Refs. [18] and [19], the original compliance matrix of the leaf-spring flexure hinge in the local coordinate is formulated by Eq. (1), where  $b$ ,  $l$ , and  $t$  are the geometric dimensions of the leaf-spring hinge, as shown in Fig. 2b.  $E$  and  $G$  are the Young's modulus and shear modulus of the material, respectively.  $k_2$  is a geometric parameter, and  $k_2 = b/t$ .

$$C_0 = \begin{bmatrix} \frac{l}{Ebt} & 0 & 0 & 0 & 0 & 0 \\ 0 & \frac{4l^3}{Ebt^3} + \frac{l}{Gbt} & 0 & 0 & 0 & \frac{6l^2}{Ebt^3} \\ 0 & 0 & \frac{4l^3}{Ebt^3} + \frac{l}{Gbt} & 0 & -\frac{6l^2}{Ebt^3} & 0 \\ 0 & 0 & 0 & \frac{l}{Gk_2bt^3} & 0 & 0 \\ 0 & 0 & -\frac{6l^2}{Ebt^3} & 0 & \frac{12l}{Eb^3t} & 0 \\ 0 & \frac{6l^2}{Ebt^3} & 0 & 0 & 0 & \frac{12l}{Eb^3t} \end{bmatrix} \quad (2)$$

The global coordinate of the DCCM is established as  $O$ - $XYZ$  in Fig. 2a. Based on the matrix transformation method, the compliance matrix of eight flexible beams is transferred from the local coordinate to the global coordinate through the following equation:

$$C_i = \begin{bmatrix} R_i & 0 \\ 0 & R_i \end{bmatrix} \begin{bmatrix} I & P_i^T \\ 0 & I \end{bmatrix} C_0 \begin{bmatrix} I & 0 \\ P_i & I \end{bmatrix} \begin{bmatrix} R_i^T & 0 \\ 0 & R_i^T \end{bmatrix} \quad i = 1, 2, \dots, 8. \quad (3)$$

For the  $i$ th flexure hinge,  $P_i = \begin{bmatrix} 0 & -r_{iz} & r_{iy} \\ r_{iz} & 0 & -r_{ix} \\ -r_{iy} & r_{ix} & 0 \end{bmatrix}$ ;

$r_i = [r_{ix} \ r_{iy} \ r_{iz}]$  is the vector from the origin  $O_i$  to the global origin  $O$  in the local coordinate  $O_i$ - $X_iY_iZ_i$ .  $R_i$  is the rotation matrix of the coordinate  $O_i$ - $X_iY_iZ_i$  with respect to  $O$ - $XYZ$ , which is decided by the rotation axis. The rotation matrixes about the  $X$ ,  $Y$ , and  $Z$  axes are

$$R_x(\theta_x) = \begin{bmatrix} 1 & 0 & 0 \\ 0 & \cos \theta_x & -\sin \theta_x \\ 0 & \sin \theta_x & \cos \theta_x \end{bmatrix},$$

$$R_y(\theta_y) = \begin{bmatrix} \cos \theta_y & 0 & \sin \theta_y \\ 0 & 1 & 0 \\ -\sin \theta_y & 0 & \cos \theta_y \end{bmatrix},$$

$$R_z(\theta_z) = \begin{bmatrix} \cos \theta_z & -\sin \theta_z & 0 \\ \sin \theta_z & \cos \theta_z & 0 \\ 0 & 0 & 1 \end{bmatrix}.$$

The stiffness matrix is the inverse of the compliance matrix. Considering the parallel connection of the eight flexible beams, the stiffness matrix of the DCCM is obtained.

$$K_{DCCM} = \sum_{i=1}^8 C_i^{-1} \quad (4)$$

The working direction of the DCCM is along the Z-direction. To maximize the working frequency, the first resonant mode shape should be better in the Z-direction, and the natural frequency in the Z-direction can be calculated as

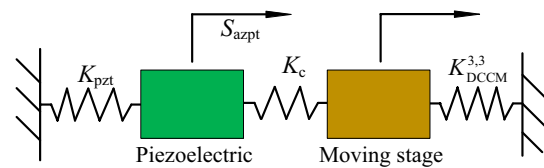


Fig. 3 Displacement output model of the piezoelectric-driven flexure-based mechanism

$$f_{\text{DCCM}} = \frac{1}{2\pi} \sqrt{\frac{K_{\text{DCCM}}^{3.3}}{M}}, \quad (5)$$

where  $M$  is the mass of the central moving stage.

### 3.2 Displacement Output of the Piezoelectric

The piezoelectric-driven DCCM is modeled in Fig. 3. The piezoelectric is seen as a mass-spring model with stiffness  $K_{\text{pzt}}$ , and an additional contact stiffness between the piezoelectric and DCCM is brought in after the piezoelectric assemble. The contact stiffness and DCCM stiffness are parallel connected to the piezoelectric, so they can be seen as the load for the piezoelectric, which leads to the reduction of the actual output of the piezoelectric. According to Hooke's law, the relationship between the nominal and actual output displacements of the piezoelectric can be calculated in the following equation:

$$S_{\text{apzt}} = \frac{K_{\text{pzt}}(K_c + K_{\text{DCCM}}^{3.3})}{K_{\text{pzt}}(K_c + K_{\text{DCCM}}^{3.3}) + K_c K_{\text{DCCM}}^{3.3}} S_{\text{npzt}}, \quad (6)$$

where  $K_c$  is the contact stiffness, and  $S_{\text{npzt}}$  and  $S_{\text{apzt}}$  are the nominal and actual outputs of the piezoelectric, respectively.

### 3.3 Stress Analysis

To guarantee the repeatability and durability of the DCCM, the stress of flexure hinges must be examined to maintain the maximum stress less than the allowable stress of the material. Considering the vertical alignment of the two-layer flexible beams, the DCCM can be seen as two parallel dual-leaf parallelogram hinges in the crossed arrangement. Thus, the stress attribution of the DCCM is similar to the parallel dual-leaf parallelogram hinges. Based on the stress analysis of the dual-leaf parallelogram hinges in Ref. [20], the maximum stress of the DCCM occurs at the up or bottom surface of the beam, and it is calculated as

$$\sigma_{\text{max}} = \frac{3k_{b1}\Delta Et}{l^2}, \quad (7)$$

where  $\Delta$  and  $k_{b1}$  are the translational displacement and stress concentration factor, respectively, and  $k_{b1} = 1.2$ .

## 4 FEA

The finite element model of the DCCM is constructed in the ANSYS Workbench software to implement the simulation analysis. The aluminum alloy is selected as the material,

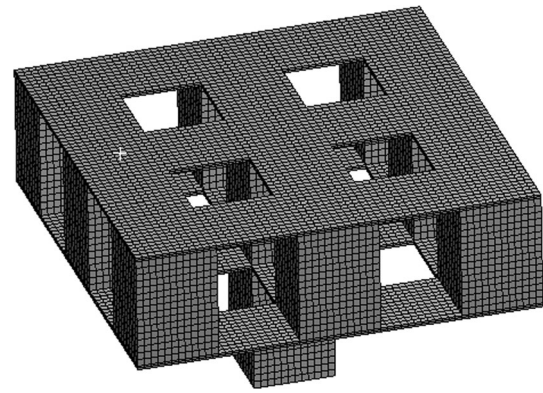
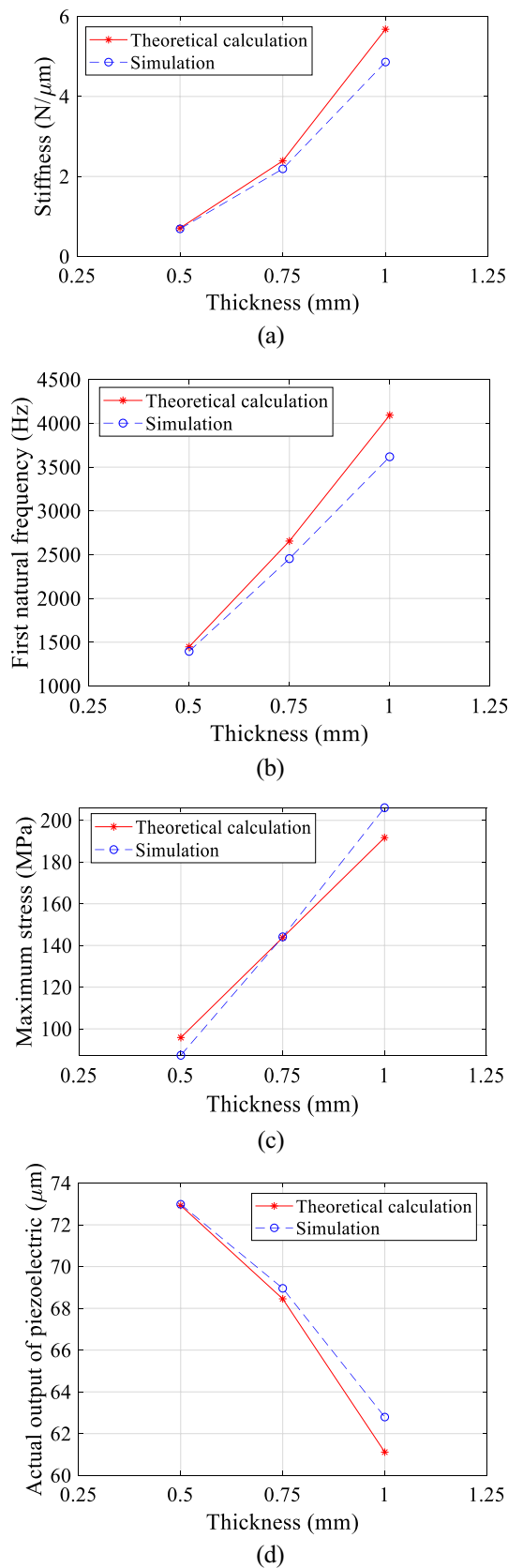


Fig. 4 Meshed double cross-shape compliance mechanism

the Young's modulus, Poisson's ratio, and density of which are 71 GPa, 0.33, and 2770 kg/m<sup>3</sup>, respectively. Considering the effect of the roller and supporting mechanism, they are equivalent to a cube with a side length of 10 mm and a height of 16 mm. The meshing quality of the flexible beam greatly impacts the simulation results for the thin thickness. Thus, the DCCM is first split into 52 separate solids with a cubic structure and then forms a new part. The free meshing of the mechanism is pretty regular, and the meshed DCCM is shown in Fig. 4.

According to the theoretical analysis, the width  $b$ , length  $l$ , and thickness  $t$  of the flexible beam and the height  $h$  affect the stiffness and resonant phenomenon of the DCCM. However, considering the boundary size of the microvibration hammerhead,  $b = 10$  mm and  $l = 10$  mm are first selected. A small height between the two layers of the cross-shape mechanisms is helpful in reducing the mass of the moving stage, which is beneficial to improve the resonant frequency. However, to conveniently preload the piezoelectric actuator and assemble the roller supporter, the distance  $h = 15$  mm is decided. Furthermore, the beam thickness greatly affects the static and dynamic properties of the DCCM, and it has little effect on the boundary size. Therefore, the effects of beam thicknesses on the stiffness, first natural frequency, maximum stress of the DCCM, and actual output of the piezoelectric are analyzed through the FEA. They are further compared to those of the theoretical analysis to validate the correctness of the established model.

Three different beam thicknesses, i.e., 0.5, 0.75, and 1 mm, are used for the analysis. The corresponding results are shown in Fig. 5. Figure 5a, b indicate that the stiffness and first natural frequency of the DCCM obviously increase as the thickness increases, and the maximum resonant frequency reaches 3618.3 Hz for the 1-mm beam thickness. However, the modeling errors of the stiffness and frequency are also increased, which are 1.38% and 3.65% for the 0.5 mm thickness, 8.67% and 8.19% for the 0.75 mm



**Fig. 5** FEA and theoretical results of the DCCM with different thicknesses: **a** Stiffness in the Z-direction; **b** First natural frequency; **c** Maximum stress; **d** Actual output of the piezoelectric

thickness, and 16.87% and 13.13% for the 1 mm thickness, respectively, which means that the compliance modeling is not applicable for the thick beam.

An input displacement of 75 μm is imposed on the center rigid of the DCCM. The simulation results show that the stress mainly occurs at the flexible beams, and the maximum stresses are shown in Fig. 5c. The simulated maximum stresses for the three beam thicknesses are 87.32, 144.13, and 206.06 MPa, all of which are less than the permissible stress of aluminum. The modeling errors between the theoretical and simulated maximum stresses are 9.77%, 0.25%, and 6.97%, and the modeling error is the least for a beam thickness of 0.75 mm. The possible reason is the applied value of  $k_{b1}$ ; a gradual change in  $k_{b1}$  is conducive to improving the modeling precision.

Based on the simulated stiffness and Eq. (5), the theoretical and simulated actual outputs of the piezoelectric are shown in Fig. 5d. When the nominal output displacement of the piezoelectric actuator is assumed to be 75 μm, the simulated actual output is reduced from 72.98 to 62.79 μm as the thickness increases from 0.5 to 1 mm, which shows the same trend as the theoretical analysis results. This is because a large beam thickness leads to a large stiffness and further reduces the displacement output of the piezoelectric, which goes against the efficient utilization of the piezoelectric.

The modal analysis of the DCCM with different beam thicknesses is further implemented, and the results are shown in Fig. 6. For the three DCCMs, the first mode shape is the translation along the Z-direction, and the second and third mode shapes are the rotation about the X- and Y-directions, respectively. Hence, the thickness does not affect the mode shape of the DCCM. In addition, the second and third natural frequencies are almost the same due to the symmetric structure. For  $t=0.75$  mm, the first three resonant frequencies are 2454.4, 10,989, and 10,989 Hz. The natural frequency of the second and third modes is approximately 4.5 times the first natural frequency, which means that the

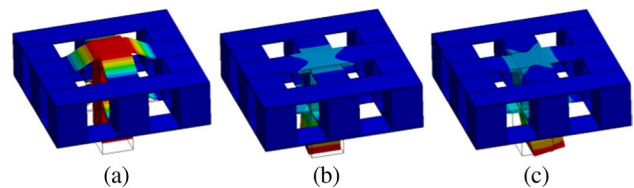


**Fig. 6** Mode shapes of the proposed hammering head. **a** First mode shape; **b** Second mode shape; **c** Third mode shape

**Table 1** Size of the DCCM

$b$	$l$	$T$	$h$	$p$
10 mm	10 mm	0.75 mm	15 mm	40 mm



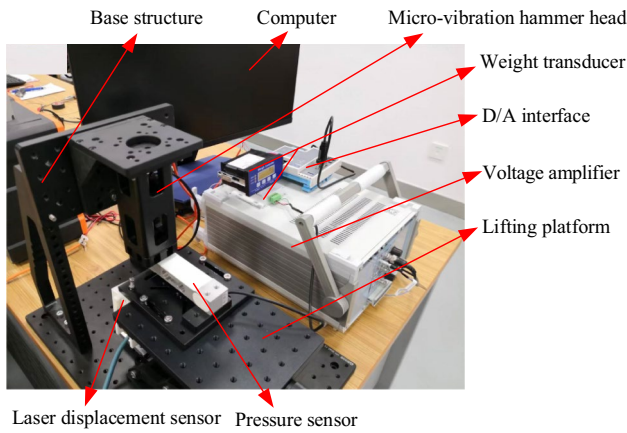


Fig. 7 Experimental setup

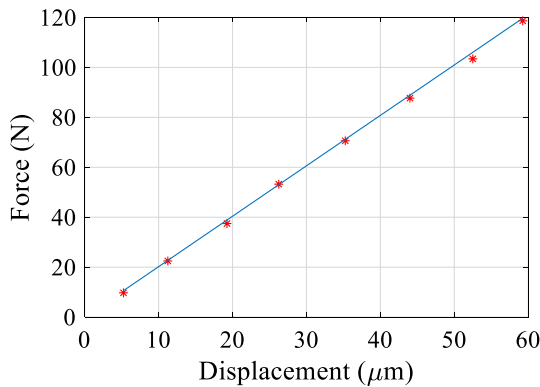


Fig. 8 Measured force and displacement

unwanted movement is hard to occur. Based on the above analysis,  $t=0.75$  mm is applied in the structure fabrication. The sizes of the DCCM are listed in Table 1.

### 5 Experimental Validation

As shown in Fig. 7, the DCCM is fabricated in a monolithic 7075 aluminum alloy using wire electrical discharge machining. A cylindrical piezoelectric (VS12, CoreMorrow) is applied as the actuator with a nominal maximum displacement of  $76 \mu\text{m}$  in 150 V. The output displacement of the piezoelectric is measured by a laser displacement sensor (CDX30, FASTUS). The LabVIEW software is employed to generate the control signal, which is first converted to an analog signal through a D/A interface (USB5820, Advantech). Then, it is further amplified 15 times by a voltage amplifier (E01.A3, CoreMorrow). A small columnar pressure sensor with a maximum range of 500 kg is applied inside the microvibration hammerhead to measure the output force of the piezoelectric.

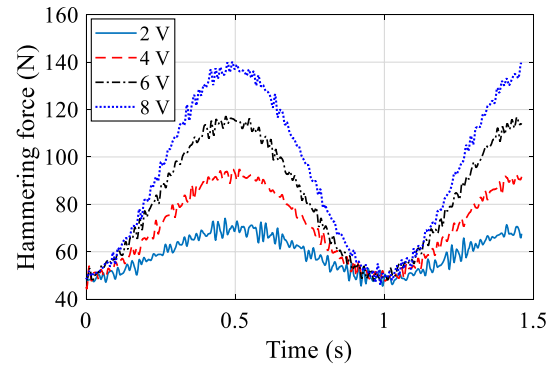


Fig. 9 Hammering force with an initial contacting force of 50 N

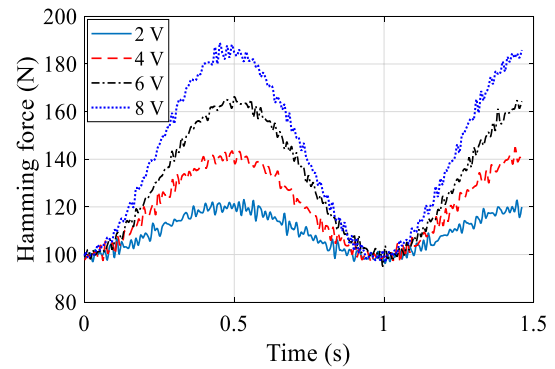


Fig. 10 Hammering force with an initial contacting force of 100 N

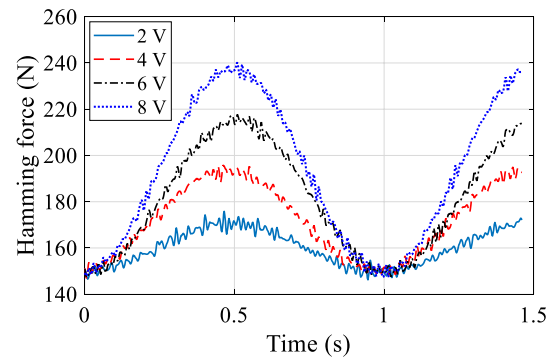


Fig. 11 Hammering force with an initial contacting force of 150 N

Different voltages of 20, 40, 60, 80, 100, and 120 V are applied to drive the piezoelectric, and the corresponding deformations of the DCCM and forces are simultaneously measured. The results are shown in Fig. 8. The stiffness of the DCCM is  $2.02 \text{ N}/\mu\text{m}$ , which agrees well with the theoretical and simulation results.

To test the resonant frequency of the hammerhead, a swept sine signal with an incremental frequency from 1 to 3500 Hz is applied to the piezoelectric actuator. The results

show that the first resonant frequency of the hammerhead is approximately 2705 Hz, which is a little larger than the FEA and theoretical results. The primary reason is that the installation of the piezoelectric brings in the contact stiffness and self-stiffness, which improves the global stiffness and further leads to a large resonant frequency.

The hammering force between the workpiece and roller is an important parameter for surface strengthening, and they are tested in this study. An external pressure sensor marked in Fig. 7 is employed to measure the hammering force, which is located under the roller. The initial contacting forces between the workpiece and roller are set as 50, 100, and 150 N, which can be adjusted by the height of the lifting platform. In the measurement of the hammering force, the deformation of the inner pressure sensor is ignored due to the large stiffness, and the deformation of the external pressure sensor is measured using the laser displacement sensor, which is used to calculate the deformation force of the DCCM and then correct the hammering force. A sinusoidal voltage signal with different amplitudes (2, 4, 6, and 8 V) and a driving frequency of 1 Hz are used to actuate the piezoelectric. The measured hammering forces are shown in Figs. 9, 10 and 11.

Based on the experimental results, the hammering force is increased with the increase in the voltage amplitude. This is because a larger driving voltage generates a larger output displacement in the roller, which further leads to a larger deformation and testing force of the pressure sensor. As shown in Fig. 9, the amplitude of the output hammering force is approximately 22.5, 45.2, 67.5, and 90.2 N for the four driving voltages, and the changing rate of the hammering force is 11.28 N/V. The same hammering force amplitude and changing rate are presented in Figs. 10 and 11, which means that the initial contacting force has little effect on the hammering force.

Based on the sinusoidal signal with an amplitude of 6 V, a series of driving frequencies (1, 10, and 20 Hz) are further inputted to the piezoelectric to investigate the influence of the driving frequency on the hammering force. As shown in Fig. 12, the amplitudes of the hammering force are 62.4, 39.4, and 19.5 N for the driving frequencies of 1, 10, and 20 Hz, and the force amplitude is significantly decreased with the increase in the driving frequency. This is mainly because the piezoelectric is similar to the capacitance, and it needs a certain amount of time for the complete charge and discharge, which directly affects the output displacement of the piezoelectric. In the high-frequency driving of the DCCM, the elongation and contract of the piezoelectric are not enough, which leads to the reduction of the output displacement, further resulting in a smaller hammering force.

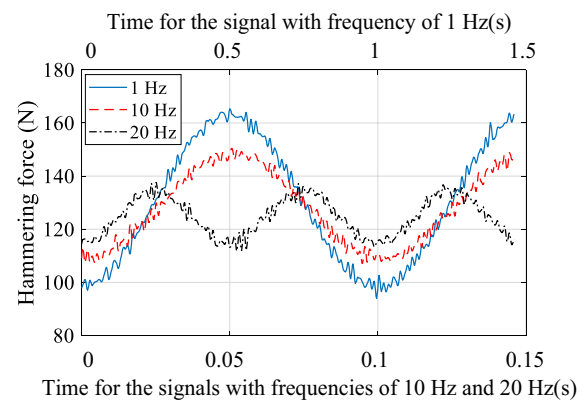


Fig. 12 Hammering force with different frequencies

## 6 Conclusions

In this paper, a novel piezoelectric-driven microvibration hammerhead is proposed, which mainly includes the piezoelectric actuator, DCCM, and inside-arranged pressure sensor. The static and dynamic properties of the microvibration hammerhead are analyzed using theoretical modeling, FEA, and experimental test. The stiffness of the DCCM is 2.02 N/ $\mu\text{m}$ , and the first natural frequency is 2705 Hz. The maximal hammering force is 90.2 N, which is affected severely by the amplitude and frequency of the input voltage but only slightly by the initial contacting force.

The proposed microvibration hammerhead will be used for surface strengthening in the future. To improve the strengthening effect and investigate the relationship between the hammering force and surface mechanical property, we will focus on the approach to improve the amplitude and precision of the hammering force.

**Acknowledgements** This research is supported by “National Natural Science Foundation of China (No. 52205138)”, “the Fundamental Research Funds for the Central Universities, CAUC (No. 3122019095)”, Science and Technology Planning Project of Tianjin Science and Technology Bureau, China (No. KJZ40420220150), Natural Science Foundation of Tianjin, China (No. 21JCQNJC00860).

**Author contributions** All authors read and approved the final manuscript.

**Availability of Data and Materials** The authors declare that all data supporting the findings of this study are available within the article.

## Declarations

**Competing Interests** The authors declare that they have no competing interests.

**Open Access** This article is licensed under a Creative Commons Attribution 4.0 International License, which permits use, sharing, adaptation, distribution and reproduction in any medium or format, as long as you give appropriate credit to the original author(s) and the source,

provide a link to the Creative Commons licence, and indicate if changes were made. The images or other third party material in this article are included in the article's Creative Commons licence, unless indicated otherwise in a credit line to the material. If material is not included in the article's Creative Commons licence and your intended use is not permitted by statutory regulation or exceeds the permitted use, you will need to obtain permission directly from the copyright holder. To view a copy of this licence, visit <http://creativecommons.org/licenses/by/4.0/>.

## References

1. Qu S, Wang J, Hu X, Lai F, Deng Y, Li X (2021) Effect of ultrasonic nanocrystalline surface modification process on fretting wear behavior of laser surface textured 20CrMoH steel. *Surf Coat Tech* 427:127827
2. Montross C, Tao W, Ye L (2002) Laser shock processing and its effects on microstructure and properties of metal alloys: a review. *Int J Fatigue* 24:1021–1036
3. Laleh M, Sadeghi E, Revilla R, Chao Q, Haghdadi N, Hugher A, Xu W, Graeve I, Qian M, Gibson I, Tan M (2022) Heat treatment for metal additive manufacturing. *Prog Mater Sci*. <https://doi.org/10.1016/j.pmatsci.2022.101051>
4. Sun X, Zhang J, Pan W, Wang W, Tang C (2022) Research progress in surface strengthening technology of carbide-based coating. *J Alloy Compd* 905(5):164062
5. Xue N, Wu Q, Zhang Y, Li B, Zhang Y, Yang S, Zhu Y, Guo J, Gao H (2023) Review on research progress and comparison of different residual stress strengthening methods for titanium alloys. *Eng Fail Anal* 144:106937
6. Attarilar B, Ebrahimi M, Hsieh T, Uan J, Gode C (2021) An insight into the vibration-assisted rolling of AA5052 aluminum alloy: tensile strength, deformation microstructure, and texture evolution. *Mater Sci Eng A Struct* 803:140489
7. Kattoura M, Mannava S, Qian D, Vasudevan V (2018) Effect of ultrasonic nanocrystal surface modification on elevated temperature residual stress, microstructure, and fatigue behavior of ATI 718Plus alloy. *Int J Fatigue* 110:186–196
8. Wang Z, Gao C, Liu Z et al (2020) Investigation of microstructural evolution in a selective laser melted Ti6Al4V alloy induced by an ultrasonic surface rolling process. *Mater Sci Eng A Struct* 772:138696
9. Li G, Qu S, Pan Y, Li X (2016) Effects of the different frequencies and loads of ultrasonic surface rolling on surface mechanical properties and fretting wear resistance of HIP Ti–6Al–4V alloy. *Appl Surf Sci* 389:324–334
10. Wang F, Zhang H, Liang C, Tian Y, Zhao X, Zhang D (2016) Design of high frequency ultrasonic transducers with flexure decoupling flanges for thermosonic bonding. *IEEE Trans Ind Electron* 63(4):2304–2312
11. Wang F, Zhao J, Lv Y, Yang Z, Gan W, Tian Z (2018) Precise vibrating electrochemical machining of a diamond-shaped hole with side-wall insulation. *Proc Inst Mech Eng C J Mech Eng Sci* 232(17):2987–2997
12. Wang L, Chen W, Liu J, Deng J, Liu Y (2019) A review of recent studies on non-resonant piezoelectric actuators. *Mech Syst Signal Process* 133(1):106254
13. Yang Z, Zhu L, Zhang G, Ni C, Lin B (2020) Review of ultrasonic vibration-assisted machining in advanced materials. *Int J Mach Tool Manuf* 156:103594
14. Lu K, Tian Y, Liu C, Zhou C, Guo Z, Wang F, Zhang D, Shirinzadeh B (2020) Design of a novel 3D ultrasonic vibration platform with tunable characteristics. *Int J Mech Sci* 186:105895
15. Lu K, Tian Y, Liu C, Guo Z, Wang F, Zhang D, Shirinzadeh B (2021) Experimental investigation of the effects of vibration parameters on ultrasonic vibration-assisted tip-based nanofabrication. *Int J Mech Sci* 198:106387
16. Wang J, Du H, Gao S, Yang Y, Zhu Z, Guo P (2019) An ultrafast 2-D non-resonant cutting tool for texturing micro-structured surfaces. *J Manuf Process* 48:86–97
17. Zhu W, Zhu Z, He Y, Ehmann K, Ju B, Li S (2017) Development of a novel 2-d vibration-assisted compliant cutting system for surface texturing. *IEEE ASME Trans Mech* 22:1796–1806
18. Guo Z, Tian Y, Zhang D, Wang T, Wu M (2019) A novel stick-slip based linear actuator using bi-directional motion of micropositioner. *Mech Syst Signal Process* 128:37–49
19. Kim H, Gweon D (2012) Development of a compact and long range XY nanopositioning stage. *Rev Sci Instrum* 83(8):085102
20. Guo Z, Tian Y, Liu C, Wang F, Liu X, Shirinzadeh B, Zhang D (2015) Design and control methodology of a 3-DOF flexure-based mechanism for micro/nano positioning. *Robot Comput Integr Manuf* 32:93–105



**Dr. Zhiyong Guo** is a lecturer in College of Aeronautical Engineering of Civil Aviation University of China. He received his Ph. D. degree in Tianjin University in 2018. His major research interests are micro-/nano-manipulation, high-precision machining technology and equipment, and surface tribology.



**Zhemin Shen** is a postgraduate in College of Aeronautical Engineering of Civil Aviation University of China. He received Bachelor's degree in Southwest Petroleum University in 2022. His major research interests are micro-/nano-driving technique and micro-electrochemical machining technology.



**Dr. Weidong Liu** is an associate professor in College of Aeronautical Engineering of Civil Aviation University of China. He received his Ph. D. degree in Tianjin University in 2020. His major research interests are electrochemical machining technology and equipment.





**Dr. Zhiqiang Zhang** is an associate professor in College of Aeronautical Engineering of Civil Aviation University of China. He received his Ph. D. degree in Tianjin University in 2018. His major research interests are additive manufacturing and surface tribology.



**Dr. Xuhao Wang** is a lecturer in Aeronautical Engineering College of Civil Aviation University of China. He received his Ph. D. degree in Tianjin University in 2020. His major research interests are robotics and mechanical dynamics.



**Dr. Lifeng Zhang** is a teacher of the School of Aeronautical Engineering, Civil Aviation University of China. He received a doctor's degree in mechanical engineering from Tianjin University in 2016. His main research directions are ultrasonic-assisted machining and precision machining technology.